Acta Biomaterialia 98 (2019) 88–102

Contents lists available at ScienceDirect

Acta Biomaterialia

journal homepage: www.elsevier.com/locate/actabiomat

Full length article

Accelerated biodegradation and improved mechanical performance of pure iron through surface grain refinement ☆

Sara Bagherifard [a,*], Mauro Filippo Molla [a], Daniel Kajanek [b], Riccardo Donnini [c], Branislav Hadzima [b], Mario Guagliano [a]

[a] Department of Mechanical Engineering, Politecnico di Milano, Milan, Italy
[b] University of Zilina, Zilina, Slovak Republic
[c] ICMATE Institute, National Research Council of Italy (CNR), Milan, Italy

ARTICLE INFO

Article history:
Received 21 January 2019
Received in revised form 7 May 2019
Accepted 11 May 2019
Available online 15 May 2019

Keywords:
Surface treatment
Severe shot peening
Biodegradation
Temporary implant

ABSTRACT

Pure iron and its biocompatible and biodegradable alloys have a high potential to be used for temporary load bearing medical implants. Nevertheless, the formation of passive iron oxide and hydroxide layers, which lead to a considerably low degradation rate at the physiological environment, has highly restricted their application. Herein we used numerical and experimental methods to evaluate the effect of severe shot peening, as a scalable mechanical surface treatment, on adjusting the performance of pure iron for biomedical applications. The developed numerical model was used to identify the range of peening parameters that would promote grain refinement on the pure iron surface. Experimental tests were then performed to analyze the gradient structure and the characteristics of the interface free surface layer created on peened samples. The results indicated that severe shot peening could notably increase the surface roughness and wettability, induce remarkable surface deformation and grain refinement, enhance surface hardness and generate high in-depth compressive residual stresses. The increased surface roughness besides the high concentration of micro cracks and dislocation density in the grain refined top layer promoted pure iron's degradation in the biologically simulated environment.

Statement of Significance: Biodegradable metallic materials with resorbable degradation products have a high potential to be used for temporary implants such as screws, pins, staples, etc. They can eliminate the need for implant retrieval surgery after the damaged tissue is healed, and result in reduced patient suffering besides lowered hospitalization costs.

Pure iron is biodegradable and is an essential nutrient in human body; however, its application as biomedical implant is highly restricted by its slow degradation rate in physiological environment. We applied a scalable surface treatment able to induce grain refinement and increase surface roughness. This treatment enhances mechanical performance of pure iron and accelerates its degradation rate, paving the way for its broader applications for biomedical implants.

1. Introduction

Temporary implants including fixation plates and wires, pins, screws, nails, staples and cardiovascular stents have the provisional function to provide mechanical support, keep the damaged parts together during the healing process or, in the case of stents, provide a transitory scaffold into the narrowed arterial vessel awaiting vessel remodelling. Usually, once the damaged tissue is healed, retrieval surgery is planned to remove these redundant metallic parts to avoid later stage complications and chronic inflammation. In these cases, biodegradable materials that can stabilize the damaged tissue and gradually dissolve with non-toxic degradation products, ideally with a pace that matches that of the tissue regeneration or remodelling, seem as a superlative solution. Considering the inadequate mechanical strength of biodegradable polymeric materials and adverse effects of their degradation products, biodegradable metallic materials have attracted collective scientific interest. Being among the essential nutrient elements playing vital roles in many biochemical reactions in the human body, magnesium, and iron are considered

☆ Part of the Special Issue associated with the 10th International Conference on Biodegradable Metals, 10th Biometal 2018, held at the University of Oxford, 26-31 Aug. 2018, organized by Professors Diego Mantovani and Frank Witte.

* Corresponding author.

https://doi.org/10.1016/j.actbio.2019.05.033
1742-7061/

as the most promising degradable metals to be used in vascular, orthopedic and craniofacial applications. However, uncontrolled and non-uniform degradation have primarily limited their application as a temporary implant material. Magnesium, in particular, has an extremely rapid degradation rate combined with the excessive hydrogen evolution and inadequate fatigue performance, which can result in premature failure [1–4]. Pure iron, on the other hand, has a slow degradation rate characterized with local pitting that highly hinders its application as bio-implant despite adequate strength and ductility (close to 316L) [5,6], and significant biocompatibility. The degradation products of iron, i.e., iron-oxides, hydroxides, carbonates, and phosphates, have been reported to be non-toxic and cytocompatible to multiple cell types [7]. The degradation of pure iron rate is so slow that it imparts a reaction similar to that of permanent implants. For instance, pure iron cardiovascular stents were reported to remain almost intact one year after implementation [8], whereas they require a degradation period of around 12–24 months [9]. Thus, appropriate approaches should be considered to modulate the degradation rate to meet the clinical requirements for biofunctionality and biosafety of these materials.

Most studies on modulating the degradation rate of iron based materials have focused on the metallurgical design of alloys trying to include elements that would induce the desired electrochemical potential [10–12]. Effects of fabrication method and microstructural texture caused by plastic deformation have also been investigated in this regard [13,14]. Porous iron structures were infiltrated by biodegradable polymers for degradation rate by inducing local acidic condition through polymer hydrolysis [15]. Surface treatments and coatings were sourced to modify the functionality of iron based materials in the biological environment. Relatively uniform and accelerated degradation rate were achieved by depositing micro patterned Au disc and Pt films on pure iron samples that served as a cathode to induce micro galvanic corrosion with the iron substrate [16,17]. There are also multiple surface coatings that despite enhancing biocompatibility, resulted in increased corrosion resistance and thus were not able to fulfil the requirements for clinical application of iron based materials [18–20]. Notwithstanding the promising results of some of the routes above, still, the sufficiently low degradation rate is not achieved for pure iron [6,17].

In this study, we use numerical and experimental approaches to investigate the potential effects of severe shot peening (SSP) on the microstructural and mechanical properties as well as electrochemical behaviour of pure iron. SSP is a low-cost surface treatment during which small spherical media accelerated by compressed air impact the target surface. The multiple impacts induce high strain at elevated strain rates, generate compressive residual stress, increase the surface roughness, and result in surface grain refinement down to nano regime [21,22]. Ultrafine and nano grains induced by various severe plastic deformation methods have been found to promote biocompatibility and biofunctionality of metallic materials [23–27]. Our previous studies demonstrated that the application of SSP on a wide range of metallic materials can enhance general mechanical performance [28–32], and inhibit bacterial adhesion while maintaining biocompatibility without inducing cytotoxicity [2,27,33]. Herein we evaluated the role of SSP in modulating the mechanical properties and biodegradability of pure iron for the first time. Pure iron has been investigated by impact based surface treatments mainly focusing on the mechanism of grain refinement. Ultrasonic shot peening (USSP) [34], surface mechanical attrition treatment (SMAT) [35–37], and Nanopeening® [38,39], have been applied to pure iron mainly to verify the extent of grain refinement, its role on nitriding mechanism and local mechanical behavior [39]. The results indicated that these treatments can induce surface grain refinement with random crystallographic orientations. The grain refinement process initiated through the formation of dense dislocation walls and dislocation tangles, which transform into sub-boundaries paving the way for the creation of highly misoriented new grain boundaries [35,36,40].

The foremost challenge for this study was to identify the apt set of SSP parameters that would result in surface grain refinement on pure iron. The main SSP process parameters are Almen intensity and surface coverage. Almen intensity is an index of kinematic energy of the shot stream and is measured as the curvature of a shot peened thin strip of SAE 1070 steel. Surface coverage is defined as the ratio of the plastically deformed surface area to the whole target area [41]; these parameters substantiate the repeatability and control of the peening process. Therefore, we first developed a numerical model of the SSP process to identify the main process parameters that could facilitate grain refinement of pure iron. Based on the results of the simulation different combinations of shot peening parameters with higher potential to promote grain refinement were selected. The samples were then shot peened and characterized regarding the effect of the applied SSP treatments on their physical, mechanical and electrochemical properties.

2. Numerical analysis and experimental procedure

2.1. Finite element simulation of the shot peening process

Numerical simulation of shot peening was implemented using finite element (FE) code ABAQUS Explicit 6.12 to develop 3D models of single and multiple shot impacts. The model consisted of a cubic body ($5 \times 5 \times 2.5\ mm^3$) representing the target material and half-spherical bodies to model the shots. The Impact area was represented by a square ($0.5 \times 0.5 \times 1\ mm^3$) located at the centre of the target top face and was meshed with fine elements defined using arbitrary Lagrangian-Eulerian (ALE) adaptive mesh strategy. The size of the elements was studied through mesh convergence analysis to ensure the independency of the results from element size. The smallest element size was adopted for each set of the treatment parameters taking into account the dimple size affected by the corresponding shot diameter and velocity. The target mesh was set up by C3D8R 8-node linear brick elements with reduced integration and hourglass control. The shots were modelled as analytical rigid bodies, considering the much higher hardness of ceramic shots with respect to the target material. The Johnson-Cook material model (Eq. (1)) was used to account for the effect of plastic strain on material hardening. The parameters of the constitutive material model are reported in Table 1, where ϵ is the equivalent plastic strain, $\dot{\epsilon}^* = \dot{\epsilon}/\dot{\epsilon}_0$ is the dimensionless plastic strain for $\dot{\epsilon}_0 = 1.0s^{-1}$, and T^{*m} is the homologous temperature.

$$\sigma = [A + B\epsilon^n][1 + C\ln\dot{\epsilon}^*][1 - T^{*m}] \quad (1)$$

$$T^{*m} = \frac{T - T_{room}}{T_{melt} - T_{room}} \quad (2)$$

In Eq. (2), T is the temperature at each time instant, T_{room} is the room temperature and T_{melt} is the melting temperature of the material. A, B, n, C, m are material constants [42]. In shot peening simulation the strain rate sensitivity is normally neglected. The bottom face of the cubic body was fully constrained, and semi-infinite elements were used to cover all the side faces of the target to avoid the reflection of propagating shear waves. Penalty contact model was considered between the shots and target material with an isotropic Coulomb friction coefficient of 0.2. The friction coefficient refers to the experimental measurements for stainless and

Table 1
Johnson-Cook parameters for pure iron [41]

A [MPa]	B [MPa]	n	m	Melting temp [K]
175	380	0.32	0.55	1811

medium carbon steel sliding against a high toughness ceria stabilized zirconia [43]. Velocity in the vertical direction was assigned as initial boundary condition to the shots, to simulate the impact angle considered in the experiments. More details on the developed FE model are available at [44,45].

2.2. Material and shot peening treatments

Samples were cut out of Armco® pure iron (99.89%) sheets of 5 mm thickness. Based on the results obtained from FE analysis, different sets of peening parameters were considered as the promising ones to model both conventionally used parameters for this material and also those that would promote grain refinement, as listed in Table 2. The main treatment parameters were gradually intensified to enhance the kinetic energy transmitted to the target material. Zirconia beads, ABZ100 (100–150 μm diameter) and ABZ850 (850–1180 μm diameter) were used as peening media to avoid contaminating the target material. Glass beads of AGB6 (53–74 μm diameter) were used just in one case to repeen the SSP treated sample and obtain more regular surface morphology with less sharp indentations. The samples were ultrasonically cleaned in acetone for 10–15 mins before each characterization test.

2.3. Surface characterization

Multiple experiments were planned to describe the surface characteristics of the treated samples. Qualitative surface morphology characterization was performed by a Zeiss EVO50 scanning electron microscopy (SEM) on random areas of one sample from each series. Quantitative surface roughness measurements were performed using a Mahr Perthometer with MFW-250 probe (tip diameter of 5 μm). Sampling and cut-off length, as well as the filtering technique, were selected following EN ISO 4287 standard. Two samples were considered per each series and measurements were performed on three different random zones of each sample. The most widely used surface roughness parameters arithmetic mean (R_a), root mean square (R_q), maximum height of the profile in the sampling length (R_z), and maximum height of the profile within the evaluation length, that is five times the sampling length, (R_t) were measured according to the definitions of ISO 4287 standard.

Sample's original microstructure and α-ferrite grain size were measured by image analysis of multiple images taken from the ground, polished and chemically etched sample. For this purpose, the sample was first impregnated in hot mounting resin, ground sequentially by SiC papers up to 2500 grit size and subsequently mirror polished using polycrystalline diamond aqueous suspension up to 1 μm. Then it was chemically etched using Nital 2% etchant. The etched sample was observed in the bright field using a Leitz Aristomet optical light microscope (OM).

Considering that the physiological solutions are aqueous based, wettability of the treated samples was verified through water contact angle (WCA) measurements performed using sessile drop technique. Two samples were considered per each series positioning small droplets of distilled water (0.7 μl) on four random positions to verify the treatments' homogeneity. The measurements were performed at room temperature.

2.4. Bulk material characterization

In-depth effect of surface treatments on microstructural features was evaluated through sample's cross-section, prepared using the same series of grinding, polishing and chemical etching method mentioned for top surface observation. The etched samples were then observed using OM in bright field mode.

To study the in-depth deformation state and grain refinement in the surface layer of the shot peened samples, electron backscatter diffraction (EBSD) analysis was performed on the samples' cross section. The samples were mechanically ground with a final polishing step using colloidal silica. A high-resolution SEM Hitachi SU70 equipped with an EBSD system was used. The inverse pole figure (IPF) maps were obtained using an acceleration voltage of 20 kV. Two magnifications were chosen to highlight the most significant differences between the bulk and the shot-peened surface. EBSD analysis was carried out on the NP, SPP5 and SSP2 samples, i.e., the samples having the extreme cases and the intermediate one regarding the shot peening parameters.

Microhardness measurements were performed in depth using a Leica-VMHT40A microhardness tester with HV0.5 indentations on three paths starting from the treated surface towards the inner parts, following ASTM E384 standard.

X-ray diffraction measurements were used to obtain the distribution of residual stresses in depth. AST X-Stress 3000 portable X-ray diffractometer (CrKα radiation ($\lambda = 2.2898$ Å)), $\sin^2(\psi)$ method, was used at a diffraction angle (2θ) around 156° corresponding to 211-reflex scanned with a total of 6 tilts in the range of −45° to 45° along three rotations of 0°, 45° and 90° with constant step size of 0.028°. Electropolishing steps were performed by Struers LectroPol5 using an electrolytic solution of 94% CH_3COOH, 6% $HClO_4$ on a circular opening of 1 cm^2. A precision Mitutoyo micrometer assured 0.02 mm depth at each removal step. Each measurement provided the mean value of residual stresses within the scanned volume, considering both the irradiated surface area and the penetration depth of the X-Ray. The latter is

Table 2
Shot peening parameters.

Sample	Shot type	Almen intensity (0.001 in.)	Surface coverage%	Repeening	
				Shot type	Coverage%
NP	–	–	–	–	–
CSP	AZB100	6N	100	–	–
SSP1	AZB100	15N	1000	–	–
RSSP1	AZB100	15N	1000	AGB6	100%
SSP2	AZB100	15N	5000	–	–
SSP3	AZB850	8-10A	1000	–	–
SSP4	AZB850	14-16A	2000	–	–
SSP5	AZB850	14-16A	6000	–	–

NP: not peened; CSP: Conventionally shot peened; SSP: Severely shot peened; RSSP: Repeened severely shot peened.

affected by mass absorption coefficient (114.57 cm^2/g) and the material density ρ (7890 kg/m^3). The penetration depth for pure iron was calculated for 99% intensity to be around 20 μm.

2.5. Electrochemical and degradation characteristics

Electrochemical impedance spectroscopy (EIS) was performed to obtain information about corrosion behavior of NP, CSP and SSP5 samples on a potentiostat VSP Biologic SAS, FR. Samples from NP series were ground by an emery paper p1000 to ensure same surface roughness across the measured area. SSP5 was selected among the SSP treated samples, based on the results obtained through the microstructural characterization tests, as will be discussed later. Standard three-electrode cell system was used with the following configuration: sample was set as working electrode, Pt electrode as counter electrode and saturated calomel electrode served SCE (+0.242 V vs. SHE) as a reference electrode. Measurements were performed at various exposure times up to 216 h to observe changes in electrochemical behaviour. The testing solution of 0.9% NaCl was used at 37 °C. This solution, known as physiological saline, simulates the concentration of chlorides in the human body environment and has been commonly used to mimic physiological fluids in biodegradation analysis of various material types [46–48]. The frequency range of EIS was set from 100 kHz to 10 mHz. Mean value of the applied sinusoidal potential was equal to open circuit potential (OCP) value and the amplitude were set to 10 mV. Obtained Nyquist plots were analyzed by the equivalent circuit method using EC Lab V10.34 software. Fig. 1 illustrates equivalent circuits used for the evaluation of Nyquist diagrams. Randels circuit (left) was used for diagrams with one capacitance loop; it suggests homogeneous electrochemical behavior across the measured surface. Circuit (in the middle) was used for diagrams with two capacitance loops, which indicates the occurrence of areas with different electrochemical behavior. The third circuit (on the right) was used for the diagrams with occurrence of Warburg impedance represented as a straight line with 45°angle. The parameter R_s represents the resistance of the solution. Constant phase element (CPE) replaces the capacitor in circuits. R_{ct} is representing charge transfer resistance and R_{cp} is the resistance of corrosion products. For a better interpretation of the data, the final resistance of surface has been designated as R_{sum}. The measurements were repeated at least three times per series. Before every electrochemical measurement, the samples from CSP and SSP5 series were pickled in a solution consisting of 36% hydrochloric acid (740 ml), hexamethylenetetramine (6 g) and deionized water (260 ml) to remove the surface oxide layer. Hexamethylenetetramine is an effective inhibitor, which protects the iron substrate from corrosion attack in acid and humid environments by redirecting the anodic reaction from the iron substrate to the dissolution of oxides formed on the surface. A detailed description of its function can be found elsewhere [49]. Potentiodynamic polarization tests were performed on the samples to verify the effect of the pickling step. In addition, cross section morphologies after 216 h of immersion in 0.9% NaCl at 37 °C were studied through SEM and optical light microscope ZEISS AXIO Imager.Z1M with camera AxioCam MRc5 and software AxionVisionRel 4.5.

2.6. Statistical analysis

All reported data refer to arithmetic means and standard deviations for at least three independent measurements, unless specified. Two-tailed student T-test was used to define statistical significance between data of multiple series.

3. Results

3.1. Numerical simulation

Initially, a single impact model was developed to perform mesh convergence analysis, after validating the correspondence of the indent size induced by the impacts with the available empirical models [50]. The results were used to define the step time required to obtain stabilized residual stress in the substrate after each impact. The multiple impact model was then developed using different combinations of peening parameters varying the Almen intensity and surface coverage. A Python code was developed to consider the randomness of the impact positions during the peening process within the target area until the defined coverage was achieved.

Fig. 2a represents the multiple impact model and a representative von-Mises stress contour in the impact area. Fig. 2b shows the in-depth distribution of residual stresses obtained from the FE analysis for a set of parameters corresponding to CSP treatment compared with the experimentally measured data. Residual stress data were extracted from the simulation averaging the values within the target area first at each layer and then in depth to consider the penetration depth of the X-ray beam. A good agreement can be observed with the in-depth distribution, while the stress values close to the surface are different from the experimentally measured data. The model was then used to assess the effect of Almen intensity and surface coverage on grain refinement. The experimental data have identified specific threshold values for equivalent plastic strain (PEEQ) as the required deformation condition to induce grain refinement in multiple severe plastic deformation techniques. Umemoto et al. [51] estimated the threshold value as a minimum required plastic strain of >7; later, Valiev suggested the required range to be >6–8 [52], that is correlated with the formation of predominantly high-angle grain boundaries. Considering PEEQ as an indicator for the initiation of nanocrystallization, we used these limit values to identify the process parameter combinations that would be more efficient in promoting PEEQ increase.

The results as presented in Fig. 3, show how the variation of surface coverage (while fixing the rest of process parameters), would affect the PEEQ evolution. Increasing surface coverage from 100% to 1000%, resulted in eight times higher surface PEEQ. The increase of Almen intensity from 6N to 8A and 16A for a fixed coverage of 100% also significantly increased the depth and maximum value of PEEQ on the top surface layer. Considering that reaching the

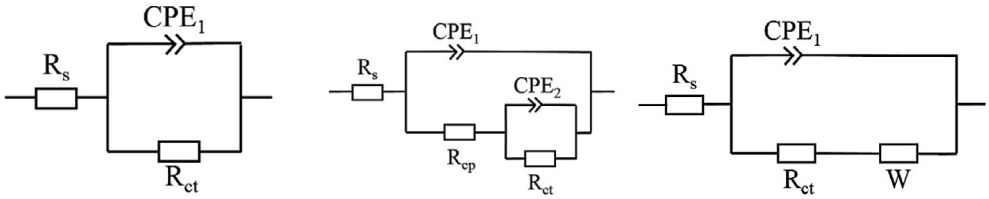

Fig. 1. The equivalent circuit used for the analysis of Nyquist diagrams.

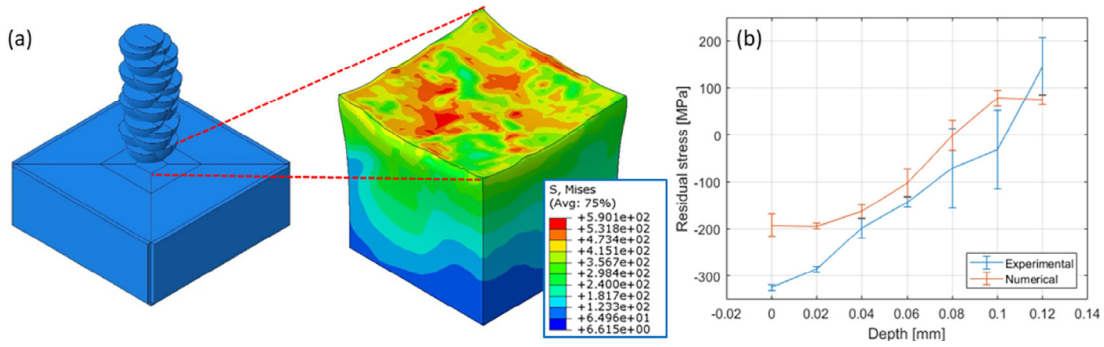

Fig. 2. a) FE model used for multiple impact analysis representing the rectangular substrate and the impinging shots and a qualitative distribution of von-Mises stress at the central impact area b) in-depth distribution of residual stresses compared with the experimentally measured data for CSP series.

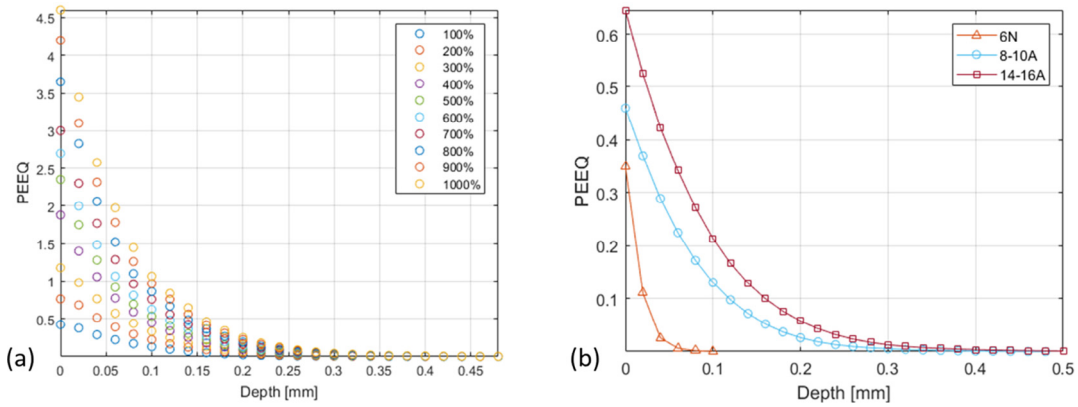

Fig. 3. a) Variation of PEEQ trend as surface coverage increases for a constant Almen intensity of 8-10A corresponding to the SSP3 treatment b) variation of PEEQ trend as Almen intensity increases, keeping the surface coverage fixed at 100%.

threshold PEEQ values is computationally costly, we used these indications, particularly the effect of surface coverage, to design our experimental campaign. Based on the observed trends, different sets of parameter combinations were planned in a way to promote the accumulation of plastic strain in the top surface layer. For the SSP series, minimum surface coverage of 1000% was considered while increasing the Almen intensity up to 14-16A to combine the stimulating effect of both parameters.

3.2. Surface characterization

Morphological top surface observations, as presented in Fig. 4, provide a qualitative indication of the effect of process parameters on the surface state. CSP series have a similar morphology to the as-received material, considering the low Almen intensity of the process. However, by notably increasing the Almen intensity and surface coverage for SSP treatments, a higher density of overlapping dimples can be observed caused by the successive impact of the shot stream. For the SSP4 and SSP5 treatments, the size of the dimples increased due to the higher diameter the media compared to all other series (850 μm vs. 150 μm).

The variation of surface roughness parameter R_a, between different series of samples, is shown in Fig. 5a and b. The rest of the parameters showed a quite similar trend (Fig. S1 in the supplementary data). NP and CSP series represented a quite similar surface roughness, while there was a sharp increase for the SSP treated samples starting from SSP1 caused by the notable change in the process parameters. The results for SSP1 and RSSP1 series indicate that the repeening process with mild parameters effectively reduced the surface roughness after SSP1 treatment. In the case of SSP3 series, a sudden drop was observed in the roughness characteristics; the highest roughness was caused by SSP5 treatment, which was characterized by the combination of highest Almen intensity and surface coverage.

Surface wettability data represented the effect of shot peening in general in promoting the interaction of the substrates with the water droplet, inducing hydrophilic characteristics. The highest wettability was obtained for SSP5 series. The SSP1 and RSSP1 samples showed distinctly different water contact angles. Also, a clear distinction was observed between wettability of NP and CSP series, despite quite similar surface roughness.

3.3. Bulk material characterization

Cross-sectional observation of different sets of samples presented in Fig. 6(b–i) represent the microstructural evolution induced by the kinetic energy of the shot peening treatment. In Fig. 6(b–i), as the kinetic energy of the process rises, through increasing Almen intensity and/or surface coverage, the thickness of the layer with modified grain structure increased. The highest kinetic energy of treatments SSP4 and SSP5 induced a dense surface layer of 40 μm and 50 μm respectively.

EBSD analysis indicated some complication in the data indexing and interpretation of areas affected by shot peening treatment due to the high deformation state and notable grain refinement in the near surface area. There are few data points close to the surface that could not be indexed, besides the voids due to the polishing artifacts that can be distinguished in the bulk. However, the overall observation of the IPF maps clearly indicated the difference in the depth of the grain refined zones on the cross-section of the sam-

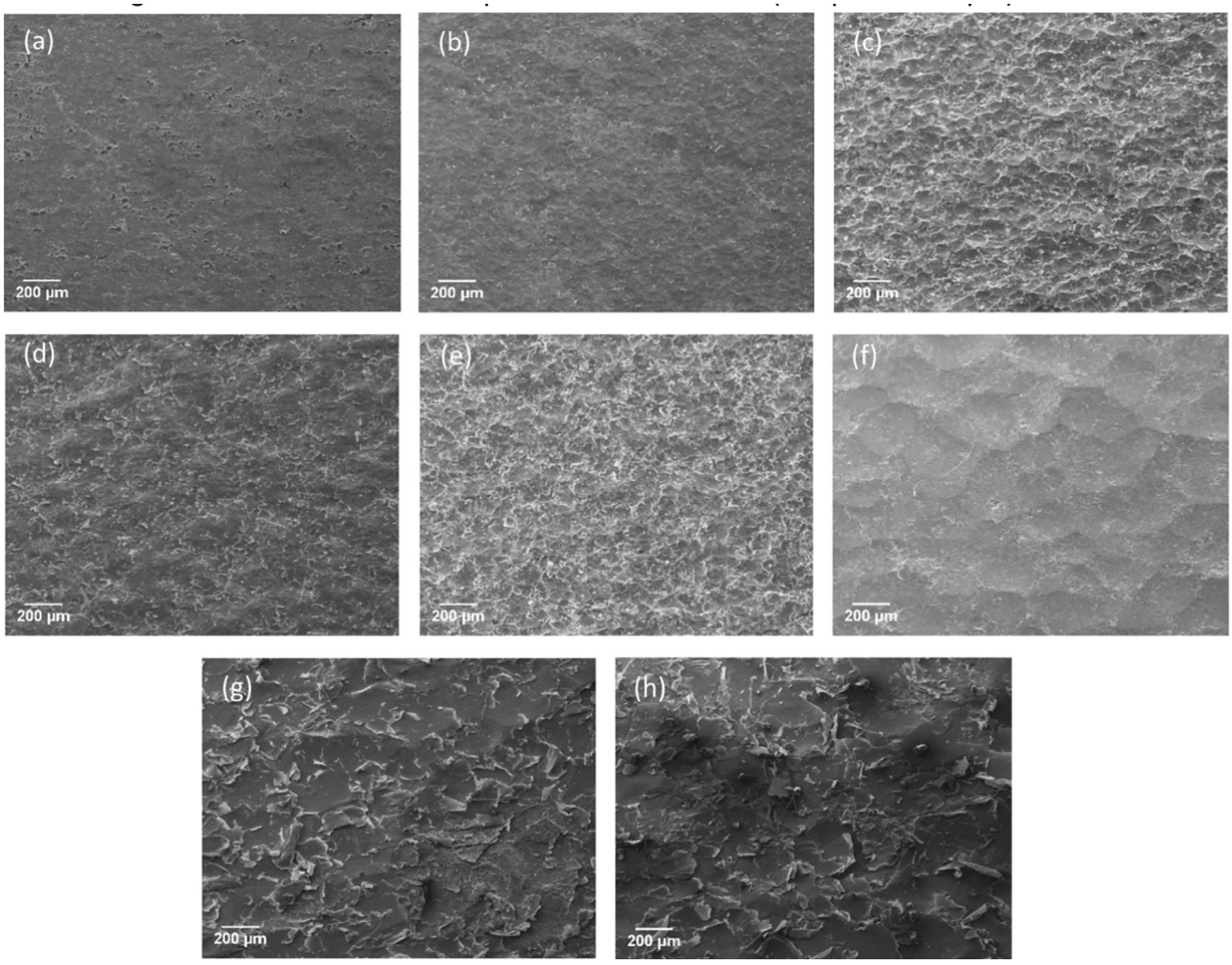

Fig. 4. Scanning electron microscopy observation of sample's top surface morphology a) NP b) CSP c) SSP1 d) RSSP1 e) SSP2 f) SSP3 g) SSP4 h) SSP5.

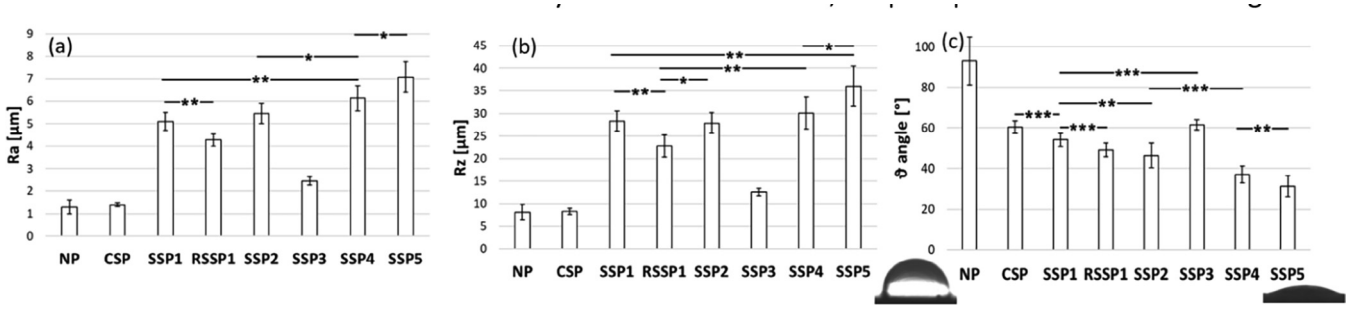

Fig. 5. Variation of surface roughness parameters among treatments a) R_a b) R_z c) Water contact angle data measured on samples' surface, the inserts refer to the water droplet on NP (right) and SSP5 (left) samples. (Data = mean ± St. Dev.; N = 6 for roughness and N = 8 for WCA, ***p-value < 0.001, **p-value < 0.01, *p-value < 0.05).

ples. The non-uniform colours in the IPF map indicate higher strain level in the grains. In the NP sample (Fig. 7a), the absence of grain refinement and deformation near the surfaces is clear at both magnifications. For the shot peened samples, the obtained IPF maps highlighted the non-uniform width of the strained layer thickness across the section. In the case of the SSP2 sample (Fig. 7b), an average minimum thickness of 20–25 µm was considered for the affected layer beyond which the grain size remained the same as the bulk material; while for the SSP5 sample (Fig. 7c) the IPF map highlighted a much thicker affected zone estimated to have a minimum average depth of 50 µm. It is noteworthy that the IPF map in Fig. 7f is characterized by an overall strained microstructural configuration, suggesting an even deeper affected layer that is highly strained.

Fig. 8c exhibits the variation of microhardness from the treated surface towards the core material for all series. The NP series demonstrate an almost constant microhardness along the depth. The microhardness variation of surface treated samples, on the other hand, had a common trend as expected for shot peened material; the highest values were observed on the top surface and gradually decreased to reach the core material microhardness. The treatment with the highest kinetic energy, i.e., SSP5 affected a

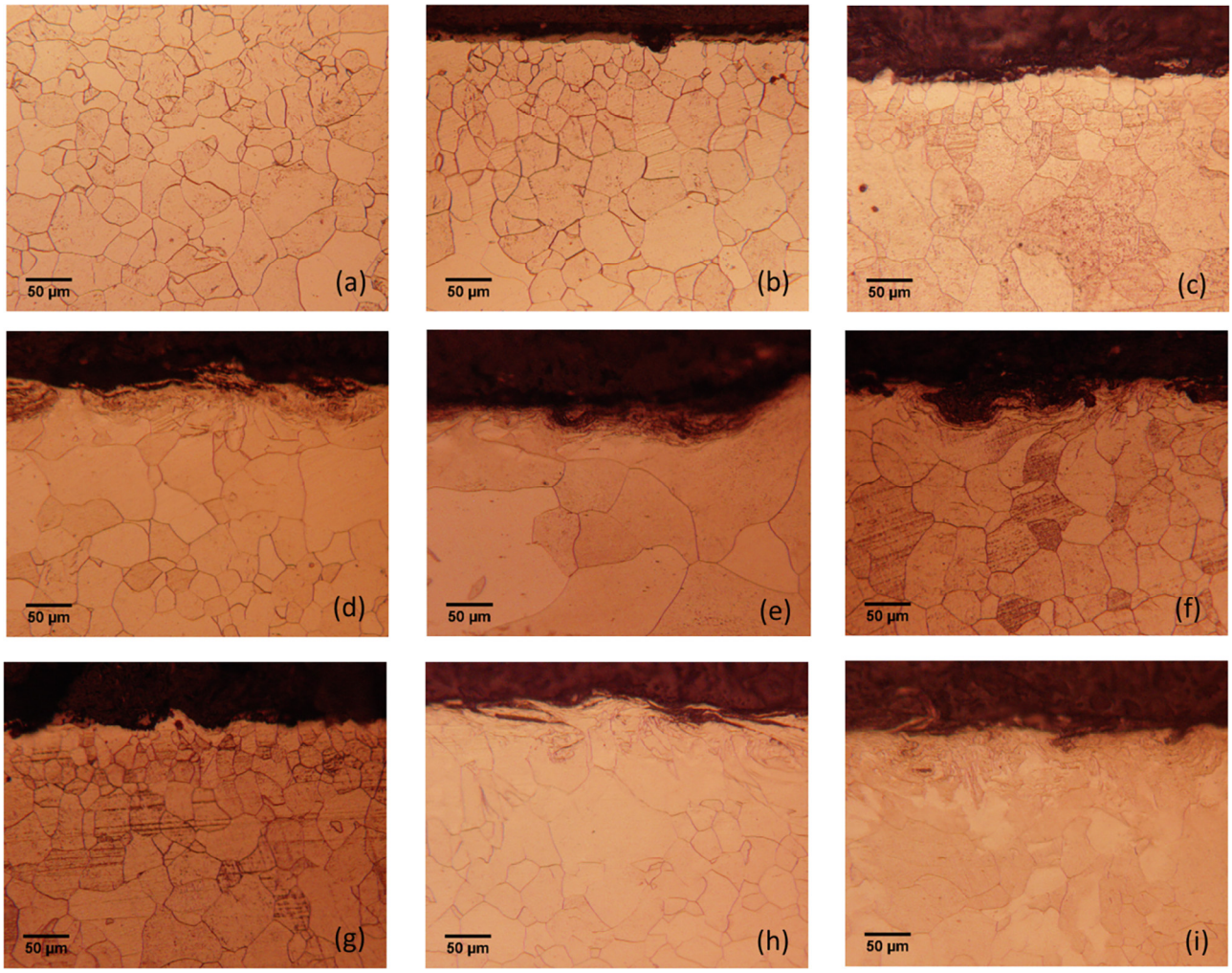

Fig. 6. a) Top surface OM observation of core material microstructure and near-surface cross-sectional OM observation of b) NP c) CSP d) SSP1 e) RSSP1 f) SSP2 g) SSP3 h) SSP4 i) SSP5 samples.

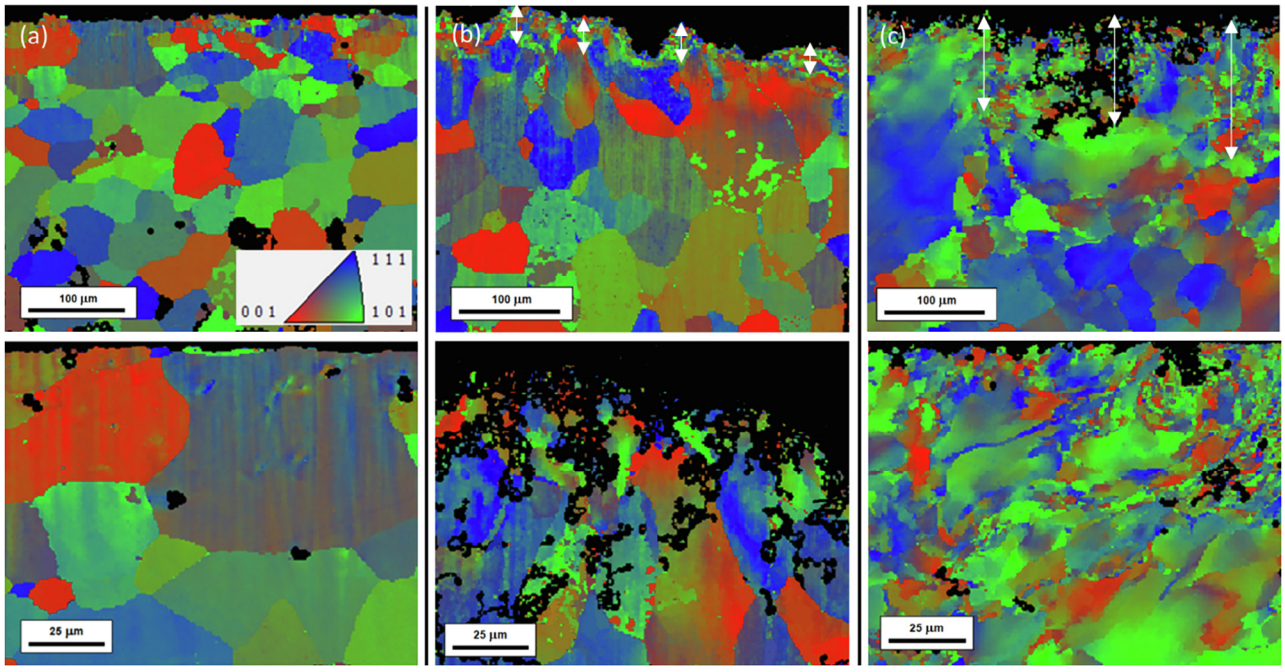

Fig. 7. IPF maps with different magnifications for a) NP b) SSP2 and c) SSP5 samples. White arrows indicate an estimation of the highly deformed and grains refined layer. Black voids in the material indicate the non-indexed areas and the ones inside the bulk can be caused by the polishing artifacts.

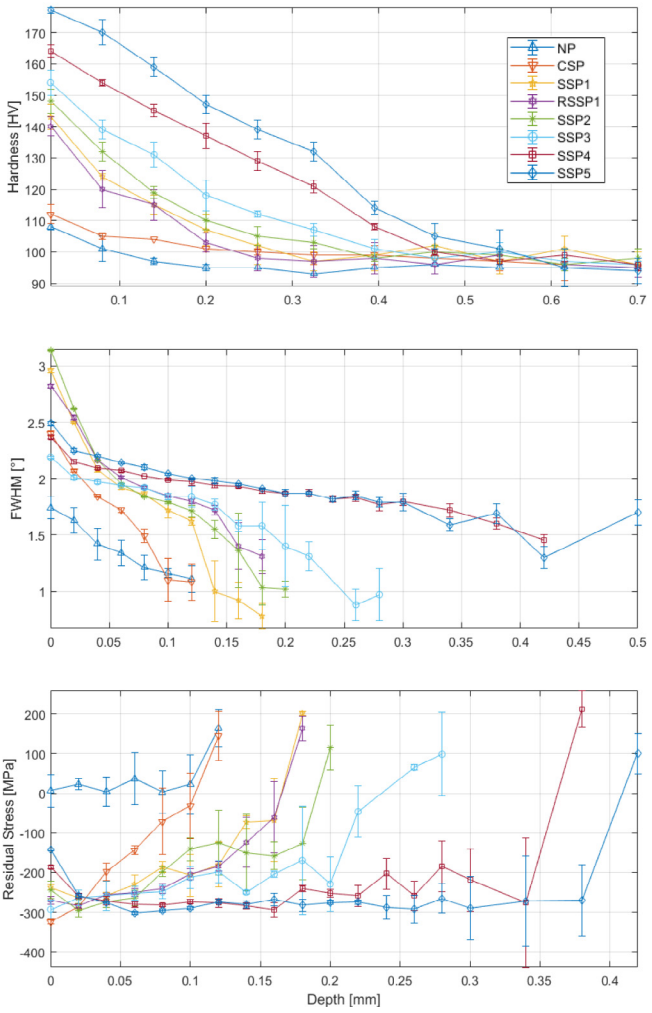

Fig. 8. In-depth distribution of a) residual stresses b) FWHM and c) microhardness values for all series.

depth of almost 600 μm with higher microhardness values with respect to the base material.

XRD measurements were performed to measure the distribution of residual stresses as well as FWHM parameter in depth (Fig. 8a-b). FWHM, the width of the diffraction peak at half the maximum intensity, is known as an index of grain refinement, microstrain, and hardness, as well as instrumental broadening. The effect of the latter is taken out by calibrating the XRD machine using strain free compact powder standard samples. The highest on-surface residual stress was obtained for CSP sample, while these series showed the smallest affected thickness with compressive residual stresses among all peened series. SSP1 and RSSP1 samples represented a similar distribution of residual stresses apart from the slightly higher depth of compressive residual stresses in RSSP1 series. The highest thickness was obtained for SSP4 and SSP5 series with a depth of 0.36 mm and 0.41 mm respectively. The maximum value of compressive residual stress regardless of the process parameters, was around 300 MPa for all series; however, the depth at which this stress reached was affected by the process parameters. Regarding the FWHM parameter, all samples represented a descending trend as the measurement point got further from the treated surface until it reached that of the base material, indicating the gradual grain refinement and work hardening effect of the applied treatments. Considering the different trends, increasing the Almen intensity and surface coverage led to a higher on-surface FWHM value and a thicker layer with FWHM higher than the base material.

3.4. Electrochemical and degradation characteristics

Three series of samples were selected based on the mechanical characterization data: SSP5 as the most promising SSP treated series, CSP as a reference to compare with the conventional treatment and NP as a control for as-received material. Measured potentiodynamic curves, shown in Fig. S2, and the data provided in Table S1 show that pickling solution successfully removed the oxide layer from CSP and SSP5 samples with higher values of corrosion density obtained after the pickling step. Nyquist diagrams of NP, CSP and SSP5 series measured in 0.9% NaCl at 37 °C are plotted in Fig. 9. The electrochemical characteristics are listed in Table 3 and the polarization resistance R_{sum} obtained using the equivalent circuit method after various exposure times are shown in Fig. 10.

In case of NP samples, R_{sum} gradually increased from 528 Ω.cm^2 after one hour of exposure up to a maximum value of 905 Ω.cm^2 after 96 h; however, the polarization resistances seemed to decrease at higher exposure times to 848 Ω.cm^2 measured after 216 h. The CSP samples represented slightly lower R_{sum} (508 Ω.cm^2) compared to NP samples after one hour of exposure. A similar increasing trend of R_{sum} was observed here; however, the maximum resistance of 1172 Ω.cm^2 was reached after 48 h. In the next exposure times, decreased R_{sum} of 885 Ω.cm^2 was measured after 168 h. CSP samples showed different electrochemical behaviour compared to NP series at 216 h, where a higher R_{sum} value (921 Ω.cm^2) compared to NP series was obtained. The SSP5 samples reached the highest R_{sum} value among all series after 1 h (658 Ω.cm^2) of exposure. Also, in this case, an intensive increase of R_{sum} values took place up to a maximum of 1051 Ω.cm^2 after 96 h. This maximum value is lower compared to the peak of CSP series but higher compared to that of NP ones. In the following stages, the polarization resistance of SSP5 sample decreased to the value of 710 Ω.cm^2 at 216 h. It can be seen that this is the lowest value compared to NP and CSP samples at the same exposure time.

Fig. S3 represents the surface of NP, CSP and SSP5 samples after 48 h of exposure in 0.9% NaCl at 37 °C. Fig. 11 shows the representative top view and cross-sectional morphologies of NP, CSP and SSP5 samples at the last time point after 216 h. After 48 h exposure the grain boundaries start to appear on the surface of the NP sample with small amount of corrosion products. The surface of the CSP sample is observed to be almost fully covered by corrosion products; while very small zones free of corrosion products could be still spotted. The SSP5 surface was locally covered by accumulated corrosion products also around the few microcracks.

The extent of areas without the presence of corrosion products are larger compared to those observed on CSP surface. The observations after 216 h exposure, indicate that the surface of the NP sample remained almost free of corrosion products confirming the low rate of iron transformation and degradation. The cross-sectional observations also confirmed less localized corrosion on the NP samples; whereas for the shot peened samples represent an increased thickness of the corrosion product layer. The top view observations of the shot peened samples (Fig. 11a–c) showed a much rougher surface morphology compared to the NP sample that was mainly induced by the original surface roughness caused by shot peening. In the case of CSP samples, corrosion products formed quite uniformly distributed on the whole exposed surface, confirmed both by the top and cross-sectional observations. The distribution of corrosion products on SSP5 sample seemed less uniform compared to CSP series; this can be attributed to the multiple overlapping surface defects and cavities on its surface that served as potential corrosion sites. The top surface observation shows

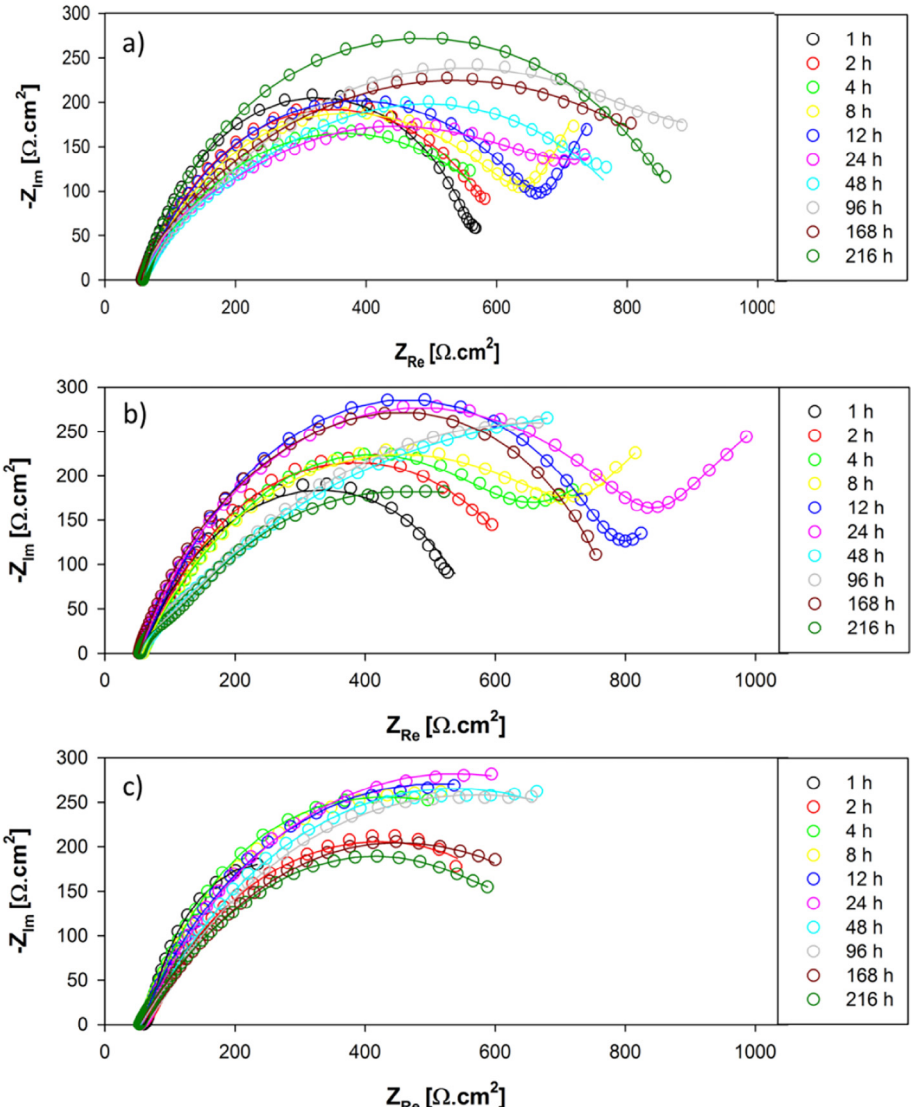

Fig. 9. Nyquist diagrams of a) NP, b) CSP and c) SSP5 samples measured in 0.9% NaCl at 37 °C.

the corrosion products were formed at a higher extent around/inside these defects. The cross-sectional observation of SSP5 samples showed some regions where the corrosion products were separated from the substrate. The Energy-dispersive X-ray spectroscopy (EDS) analysis performed on the surface of treated samples did not indicate any significant difference in the surface composition of the different samples. This negated the presence of any ceramic traces that could have remained on the surface from the fragmentation of the ceramic shots. At any rate, although the possible residuals of ceramic could have acted as the cathodic site in a micro galvanic corrosion, the difference between the surface area covered by the potentially embedded particles and the metallic surface was so high that any possible effects could be very marginal and negligible; also keeping in mind that minimal amounts of ceramic could be totally covered by corrosion products at the initial phases of corrosion.

4. Discussion

In this study, we proposed SSP as a scalable and low-cost mechanical surface treatment with a high potential to modulate microstructural, mechanical and degradation behaviour of pure iron. The developed FE model served as a predictive tool to identify the influence and the range of the primary process parameters that would uphold grain refinement. The model was validated through comparison with experimental residual stress measurements. The slight difference of the on-surface stresses between the numerical and experimental data could be partially related to the significant surface roughness of specimens. The high points in the rough surface contribute more to the XRD pattern and can introduce some errors to the measurements on the first layers. The error decreased on sub-surface points where a smoother surface was obtained by electropolishing. To induce high PEEQ values on the surface layer without introducing major surface defects, the experimental parameters were selected using a minimum surface coverage of 1000% for SSP treatments, while maintaining the Almen intensity in the range used in the FE simulations. This was to take into account the effect of excessively high Almen intensity in increasing the density of surface defects and microcracks.

Qualitative SEM observation of the surface morphology indicated multiple overlapping dimples on the top surface of the treated samples; the width of the dimples enlarged as the media size, and Almen intensity increased. Quantitative surface roughness measurements also indicated a notable increase in the surface roughness as the kinetic energy of the process increased. The peen-

Table 3
Electrochemical characteristics of NP, CSP and SSP5 series after various exposure times in 0.9% NaCl at 37 °C.

NP	R_s (Ω.cm^2)	R_{CP} (Ω.cm^2)	R_{CT} (Ω.cm^2)	R_{sum} (Ω.cm^2)	CPE1 (F.s^{n-1})	CPE2 (F.s^{n-1})	n1	n2	W (Ω.$s^{1/2}$)
1 h	56 ± 2	–	528 ± 35	528 ± 35	4.30E-04 ± 0.3E-04	–	0.79 ± 0.12	–	–
2 h	57 ± 1	–	578 ± 27	578 ± 27	5.80E-04 ± 0.5E-04	–	0.72 ± 0.13	–	–
4 h	55 ± 1	–	629 ± 41	629 ± 41	5.90E-04 ± 0.3E-04	–	0.73 ± 0.08	–	–
8 h	57 ± 2	–	671 ± 39	656 ± 39	5.50E-04 ± 0.2E-0.4	–	0.68 ± 0.04	–	39 ± 5
12 h	57 ± 1	–	677 ± 13	677 ± 13	6.90E-04 ± 0.2E-0.4	–	0.69 ± 0.03	–	24 ± 3
24 h	57 ± 1	–	750 ± 27	750 ± 27	9.80E-04 ± 0.6E-0.4	–	0.71 ± 0.04	–	19 ± 1
48 h	56 ± 1	–	820 ± 71	820 ± 71	1.17E-03 ± 0.03E-0.3	–	0.57 ± 0.02	–	–
96 h	55 ± 1	–	905 ± 112	905 ± 112	1.16E-03 ± 0.03E-0.3	–	0.58 ± 0.02	–	–
168 h	55 ± 3	–	856 ± 79	856 ± 79	1.26E-03 ± 0.09E-0.3	–	0.61 ± 0.03	–	–
216 h	58 ± 2	–	848 ± 29	848 ± 29	8.50E-04 ± 1.1E-0.4	–	0.74 ± 0.06	–	–

CSP	R_s (Ω.cm^2)	R_{CP} (Ω.cm^2)	R_{CT} (Ω.cm^2)	R_{sum} (Ω.cm^2)	CPE1 (F.s^{n-1})	CPE2 (F.s^{n-1})	n1	n2	W (Ω.$s^{1/2}$)
1 h	58 ± 1	–	508 ± 59	508 ± 59	8.70E-04 ± 1.1E-04	–	0.74 ± 0.07	–	–
2 h	58 ± 1	–	663 ± 66	663 ± 66	1.21E-03 ± 0.11E-03	–	0.71 ± 0.03	–	–
4 h	58 ± 1	–	755 ± 95	755 ± 95	1.18E-03 ± 0.06E-03	–	0.65 ± 0.03	–	44 ± 5
8 h	57 ± 2	–	813 ± 46	813 ± 46	8.50E-04 ± 0.5E-04	–	0.66 ±0.04	–	61 ± 9
12 h	55 ± 2	–	841 ± 61	841 ± 61	9.70E-04 ± 0.5E-04	–	0.73 ± 0.02	–	31 ± 4
24 h	54 ± 2	–	847 ± 45	847 ± 45	4.50E-04 ± 0.4E-04	–	0.73 ± 0.06	–	34 ± 3
48 h	54 ± 1	72 ± 10	1100 ± 255	1172 ± 265	3.57E-06 ± 0.5E-06	3.86E-03 ± 1.2E-03	0.63 ± 0.01	0.59 ±0.04	–
96 h	55 ± 2	49 ± 2	1098 ± 241	1147 ± 243	2.26E-03 ± 0.13E-03	3.90E-03 ± 1E-03	0.75 ± 0.04	0.58 ±0.03	–
168 h	54 ± 1	51 ± 3	834 ± 188	885 ± 191	1.34E-03 ± 0.07E-03	5.78E-03 ± 1.8E-03	0.91 ± 0.05	0.61 ±0.02	–
216 h	55 ± 2	38 ± 2	883 ± 150	921 ± 152	4.60E-04 ± 1.1E-04	4.65E-03 ± 1.5E-03	0.92 ± 0.03	0.63 ±0.04	–

SSP5	R_s (Ω.cm^2)	R_{CP} **(Ω.cm^2)**	R_{CT} (Ω.cm^2)	R_{sum} (Ω.cm^2)	CPE1 (F.s^{n-1})	CPE2 (F.s^{n-1})	n1	n2	W (Ω.$s^{1/2}$)
1 h	56 ± 1	–	658 ± 41	658 ± 41	2.80E-02 ± 0.43E-02	–	0.79 ± 0.11	–	–
2 h	57 ± 1	–	734 ± 61	734 ± 61	2.50E-02 ± 0.39E-0.2	–	0.67 ± 0.04	–	–
4 h	55 ± 1	–	864 ± 126	864 ± 126	4.67E-03 ± 0.12E-03	–	0.65 ± 0.01	–	–
8 h	56 ± 2	–	937 ± 139	937 ± 139	6.97E-03 ± 1.2E-03	–	0.69 ± 0.03	–	–
12 h	56 ± 2	–	951 ± 115	951 ± 115	6.40E-03 ± 0.6E-03	–	0.68 ± 0.06	–	–
24 h	56 ± 2	–	997 ± 40	997 ± 40	5.34E-03 ± 0.33E-0.3	–	0.66 ± 0.03	–	–
48 h	55 ± 1	–	1020 ± 190	1020 ± 190	3.59E-03 ± 0.64E-0.3	–	0.61 ± 0.06	–	–
96 h	54 ± 2	–	1051 ± 141	1051 ± 141	3.64E-03 ± 0.51E-03	–	0.58 ± 0.03	–	–
168 h	53 ± 1	–	768 ± 69	768 ± 69	3.40E-03 ± 0.41E-0.3	–	0.58 ± 0.03	–	–
216 h	53 ± 1	–	710 ± 44	710 ± 44	3.16E-03 ± 0.22E-03	–	0.59 ± 0.02	–	–

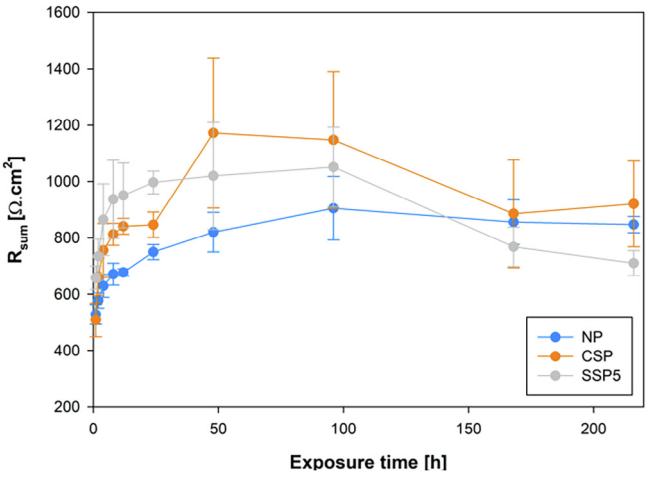

Fig. 10. Electrochemical characteristics of NP, CSP, and SSP5 series after various exposure times in 0.9% NaCl at 37 °C.

ing media characteristics highly affected the dimple size and therefore the surface morphology and roughness, considering that an apparent drop in the trend was observed as the peening media dimension changed from 150 μm to 850 μm. This observation implied the importance of the peening media choice, independent from other parameters that affect the kinetic energy of the peening process.

Surface wettability measurements were performed using distilled water droplets as a valid choice to simulate the interaction with aqueous physiological solutions [53–55]. The analyses indicated quite similar results on random surface locations highlighting that the surface treatments led to a rather uniform effect despite the randomness of the multiple impacts. Shot peening, generally, upheld the interaction of the samples with the water droplet. The highest wettability among all the treated series, observed on SSP5 series, could be due to the combination of grain refinement and the increased surface roughness; since these two aspects are known to have a synergistic contribution in surface wettability [33]. The increasing trend of wettability was disrupted with the two exceptions: RSSP1 and SSP3 series. Being selected to be a quite mild peening process just to slightly flatten the highest peaks, repeening is not expected to affect the grain size, as confirmed in our previous studies [2,33]. Thus, the decrease in WCA for RSSP1 compared to SSP1 series could be largely attributed to the reduced surface roughness. However, the SSP3 series, show increased WCA despite lower surface roughness that abruptly drops due to the noted change of shot diameter with respect to the previous series. Moreover, NP and CSP samples showed a quite different WCA but similar surface roughness parameters. Thus, it seems that there is not a direct trade-off between surface roughness and WCA. That could be justified by the different morphology of the sample's surface that is not necessarily projected in standard surface roughness parameters. Comparison of surface morphologies presented in Fig. 4, reveals a more smooth surface morphology within the dimples for SSP3 series compared to the other samples. The same goes for NP and CSP series that present quite different surface morphology but comparable roughness data. As reported in previous studies, the surface features that determine surface morphology, seem to have a more significant role in dictating the interaction of the material with the surrounding environment, particularly with the wetting media and proteins present in the biological environments, compared to the roughness parameters defined based on amplitude parameters [33,56]. These standard

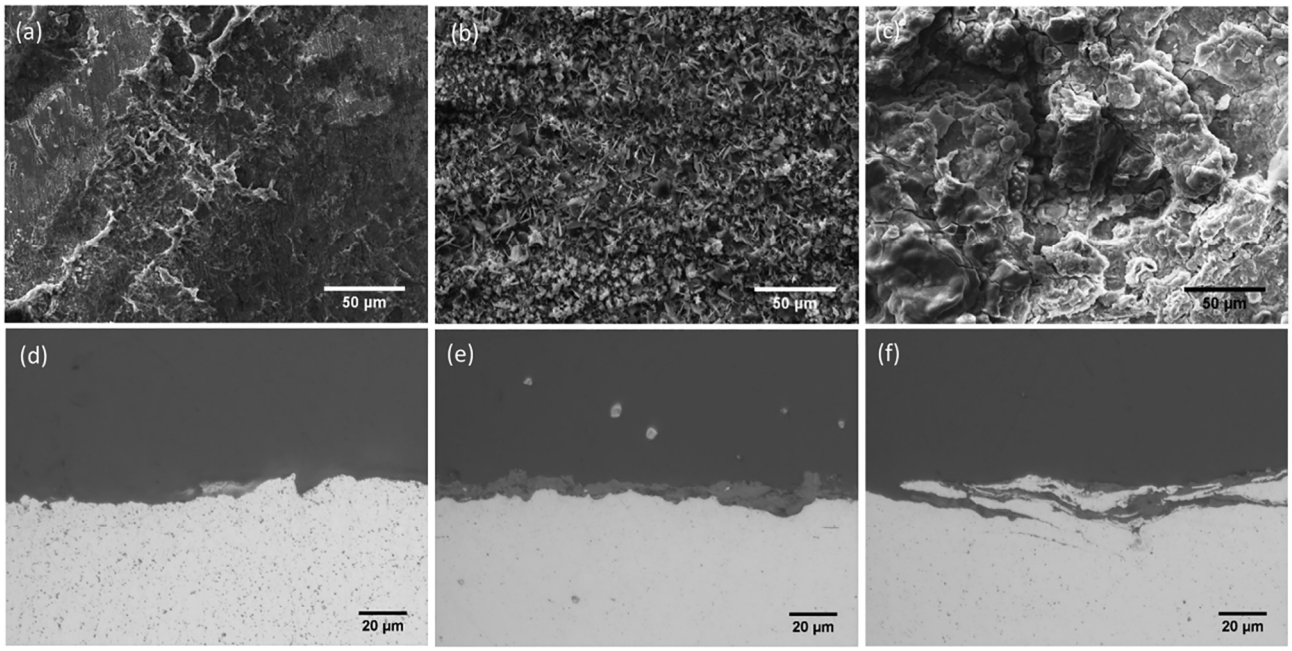

Fig. 11. Representative top (top row) and cross-sectional (bottom row) morphologies of a) NP, b) CSP and c) SSP5 samples after 216 h of exposure in 0.9% NaCl at 37 °C.

parameters, although widely used, are not able to provide an accurate description of the surface morphology including the formation of irregularities and their spatial distribution. Thus, we postulate that these morphological differences could have been responsible for the deviation in the trend of WCA variation as the kinetic energy of the process increases.

Top surface microstructural observation of the as-received material, shown in Fig. 6a (NP), represented a homogeneous structure of equiaxed crystals. Image analysis performed on 100 individual grains randomly selected on 10 different samples provided original grain size estimation around 42 ± 6 µm; this was also confirmed by EBSD analysis. In the cross-sectional micrographs, all the shot peened series exhibited a quite dense and highly deformed top surface structure, the thickness of which enlarged as the kinetic energy of the applied process increased. The highest thickness was measured to be around 50 µm for SSP5 treatment that had the highest kinetic energy. The IPF maps obtained from the EBSD analysis underlined the highly strained microstructural state of the near-surface layer for the shot peened samples. The apparent increase in the depth of the grain refined layer by increasing the kinetic energy of the process from SSP2 to SSP5 again indicated the importance of the choice of shot peening parameters.

The grain refinement process is dictated by the plastic deformation mechanism and dislocation activities that are known to be affected by the lattice structure and the magnitude of the stacking fault energy. Depending on these characteristics, polycrystalline materials will accommodate plastic strains by triggering multiple dislocation activities, including sliding, accumulation, interaction, tangling, and spatial rearrangement [35]. In pure iron, as a material with a high stacking fault energy, experimental observations under large plastic strain have revealed that dense dislocation walls and dislocation tangles are formed inside the grains. The latter creates individual dislocation cells in the original grains separated by dense dislocation walls and tangles. Upon further plastic deformation, these features will transform into sub-boundaries with small misorientation through annihilation and rearrangement. The subgrain boundaries will later evolve into high angle grain boundaries, splitting the coarse grains into smaller size ones [35,57]. The dimension of dislocation cells generated inside the original grains is a function of the acting shear stress [58]. Thus, it is expected that increased shear stress, results in increased lattice dislocation density, smaller dislocation wall spacing and therefore more refined cell sizes. There are indications that multidirectional impacts obtained in USP treatment may promote the grain refinement process. The positive effect of shear strain in the form of tilted angle adopted in micro-percussion tests is also reported to emphasize the significant role of shear bands induced by shearing contact process during repetitive inclined indentation in grain refinement of pure iron [59]. Accordingly, it is expected that the combination of shearing contact with normal impact could promote the microstructural transformation of pure iron during SSP treatment. Further investigations are in course to validate this hypothesis.

The microhardness results indicated that increasing the kinetic energy of the shot peening process, led not only to higher surface hardness but also to a higher depth of the altered zone depending both on the applied intensity and coverage. Following the Hall-Petch equation, the significantly increased surface microhardness can be due to the notable grain refinement compared to the inner areas [60]. The quite similar trend of SSP1 and RSSP1 series confirmed that the slight repeening process did not affect the microhardness of the material but just influenced the surface topography.

In-depth distribution of residual stresses was highly affected by shot peening parameters. The maximum compressive residual stress value observed for all SSP treatments was similar and higher than the yield stress of the material (Table S2 and Fig. S4). The yield strength of the material should limit the equivalent von-Mises residual stresses induced in the material. The difference observed between the residual stresses and the yield stress of pure iron could be attributed to the strain hardening happening in the subsurface layer due both to the not perfectly elasto-plastic static behavior of the material and to the loading–unloading cycles that the material underwent during the multiple sequential impacts. The hardening induced by the sensitivity of pure Fe to the strain rate could also lead to increased local yield strength. This could further displace the limit for the maximum equivalent stress that can be reached for the material. It is also to be noted that the state of the stress in-depth is tri-axial and the third component that cannot

be measured by XRD, might also contribute in decreasing the equivalent residual stress in depth compared to what we calculated by just in-plane stress components. While the maximum compressive residual stress is not influenced by the SSP parameters, the depth with compressive stresses is strongly affected due to the different global amount of energy introduced in the material by each set of process parameters.

Compressive residual stresses are particularly of utmost interest for their ability to reduce crack propagation rate under cyclic loading and are known to highly promote fatigue strength [28,29,61]. Refined grain size, on the other hand, is expected to defer crack initiation or alter the crack initiation mechanism and hence improve the fatigue strength [62]. Contrary to the latter parameters that are expected to enhance fatigue performance, the increased surface roughness and surface defects generated in the topmost layers can deteriorate the fatigue performance. Previous results have indicated that the adverse effect of surface defects and surface roughness can be overshadowed by the deep residual stress field and the grain refined layer [2]; however, detailed fatigue tests should be performed to assess the synergistic effect of all these parameters in the fatigue performance of the SSP treated pure iron.

FWHM is affected by variation in microstructure and stress–strain accumulation; it can be regarded as a cumulative index of plastic deformation, dislocation density, and hardness [63]. Higher Almen intensity and surface coverage were found to result in increased on-surface FWHM and a thicker layer characterized with higher FWHM than the base material. The declining trend of FWHM with the highest value on the top surface for all samples can be regarded as an indication of gradient grain size and the reduction in the extent of work hardening.

The Nyquist diagrams and the values of polarization resistance for all samples indicated continuously increasing resistance in the early exposure times, followed by a drop in the resistance at later stages. This trend can be attributed to the interaction between the sample's surface and the electrolyte, which led to the creation of corrosion products. The corrosion product layer could act as a barrier against aggressive chloride ions contained in the electrolyte, and lead to an increase in the R_{sum} values. After reaching a critical point, the values of R_{sum} started to decrease till the end of the measurements. This could be explained by possible occurrence of surface defects and micro-cracks in the corrosion product layer through which electrolyte was able to penetrate towards the iron substrate. We postulate that as the exposure time increased, the thickness and weight of the corrosion product layer was enlarged because of ongoing anodic reaction. However, this assumption should be quantitatively verified by adapting an efficient weight loss measurement strategy.

The main difference of corrosion behaviour between the samples, however, was the R_{sum} variation in both the growing and declining phases that are more notable for shot peened series; for example, SSP5 sample reached the highest values of R_{sum} after each time point up to 24 h. Shot peening is known to lead to notable surface deformation, increased dislocation density, and induction of compressive residual stresses. It is well known that these factors can adversely affect the corrosion resistance of material as they highly increase the surface activity [2,64]. CSP cross section (Fig. 11e), illustrates the presence of a quite uniform layer of corrosion products, which protects the substrate against harmful chloride ions and therefore increases the corrosion resistance, showing higher R_{sum} compared to the NP series at the early stages. Faster growth of corrosion products takes place on SSP5 sample giving rise to higher surface protection at the early stages. Then again, the rapid growth of corrosion products leads to earlier attainment of their critical weight, resulting in earlier detachment and felling of the products and thus uncovering the samples' surface. This is also confirmed by the cross-sectional observation of SSP5 sample (Fig. 11f) where the corrosion product layer does not exhibit a uniform distribution through the sample's surface. After this time point, the R_{sum} values of SSP5 sample tend to decline progressively showing the lowest corrosion resistance. These observations can be directly attributed to the kinetic energy of the shot peening process. Unlike the CSP sample, the surface layer of SSP5 has a higher surface roughness (Fig. 5a-b) and contains numerous defects and microcracks. The latter can offer additional space for electrolyte permeation and act as preferential corrosion sites amplifying the active surface area. Anodic reactions were promoted at the peaks of rough surface/outside surface cracks, filling the latter with corrosion products. Continuous corrosion reactions on the surface layer and inside the surface microcracks can promote delamination of the corrosion products and thus expose the underlying layer once again to the corrosive environment. As this cycle continued, the SSP treated sample demonstrated a lower corrosion resistance compared to the other series. Indeed considering the scatter range in the corrosion resistance data, there is no significant difference in R_{sum} between different series especially at lower exposure times. We assume that the high scatter could have been due to the randomness in the surface irregularities of the shot peened series, as the NP sample, in most cases showed lower scatter range compared to the shot peened ones. However, the scatter ranges tend to become more limited at higher exposure times. For the last time point, differences of 17% and 20% could be detected between SSP series and the results for NP and CSP series respectively.

As reported in Table 3, the parameter n varied within the range of 0.57–0.9 for all of the measurements. Therefore the capacitor had to be replaced by a constant phase element CPE. It is also necessary to point out that the CPE behavior can be characterized between Warburg impedance (n = 0.5) and capacitor (n = 1). Variation of CPE across all time points for all the samples is shown in the Fig. 12. According to the Amirudin and Thierry [65], A_d parameter represents an electrochemically active area or delaminated area and it is given by ratio in Eq. (3), where $C_d$is the double layer capacitance and C_d^0 is the area-specific double-layer capacitance of the uncoated metal.

$$A_d = \frac{C_d}{C_d^0} \tag{3}$$

If we consider that the electrochemically active area is in direct relation with C_d (in our case replaced by CPE), then it can be stated that at initial exposure times, CPE of NP, CSP and SSP5 followed the

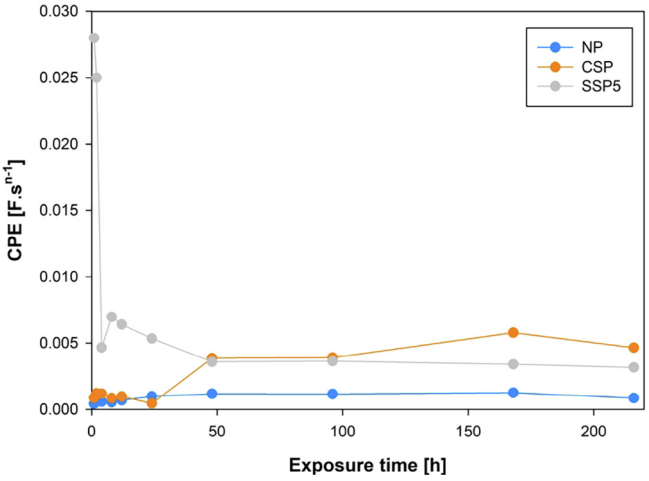

Fig. 12. Variation of CPE for NP, CSP and SSP5 samples after various exposure times in 0.9% NaCl.

same trend as the roughness measurements; i.e. the highest roughness resulted in the highest electrochemically active area measured for SSP5 and the lowest value obtained for the NP sample. During exposure, CPE of SSP5 sample was drastically decreased in the first 4 h due to the coverage of rough surface caused by anodic reaction concentrated on the surface peaks. In this case, the formation of corrosion products was concentrated in the dimple areas where cathodic reaction took place. The CPE of the CSP specimen did not change significantly up to 48 h of exposure. After 48 h, the layer of corrosion products was sufficiently compact and thus the second semicircle was detected (the presence of second time constant) for CSP sample. This appearance could be related to the continuous coverage of the surface by corrosion products. It is supported by the increment of CPE values observed at the final exposure times. In the case of NP sample, an increase (although not so significant as in the case of CSP) took place due to the larger area of the surface caused by etching-like corrosion process (Fig. S5). Whole grains were attacked by the corrosive environment, and this is probably the reason why corrosion products were not clearly observed at the end of measurement on NP sample and that the surface displayed an etched-like morphology with the very limited appearance of corrosion products (Fig. S5). The different behavior observed in the case of CSP and SSP5 samples could be due to the compressive residual stresses in the surface layer, which compressed the grains together. Moreover, the grain size in the top surface layer of the shot peened series was quite small, and thus probable etching was not as observable as in case of NP series. At certain exposure times in case of NP and CSP samples, diffusion processes were observed at the low-frequency region of Nyquist diagrams due to the detection of a straight line with a slope of 45°. According to [66] this could be due to the fact that oxidizing or reducing potentials were held long enough to cause the depletion of the species in front of the electrode.

The results of the electrochemical tests are in good agreement with a study on the effect of sand blasting on corrosion resistance of pure iron, where the sand blasted samples showed significantly different electrochemical behaviour compared to the bare iron after three days of immersion in simulated body fluid [64]. We postulate that the deciding factors in the accelerated corrosion are i) the induced surface morphology and increased surface roughness that amplify the exposed surface (including dimples and microcracks) and ii) the presence of grain refined layer characterized by a high dislocation density and high electrochemical activity that promotes rapid formation of a protective corrosion product layer. Besides, the adhesion of this protective layer is troubled with the high surface roughness, and its fast growth fuels its breakdown and detachment from the substrate. The effect of these parameters on the degradation mechanism is highly symbiotic making it quite complex to distinguish the individual role of each factor. Increased surface roughness is recognized to amplify the effective area and active sites for electrochemical reactions. The increased dislocation density induced by plastic deformation is considered to reduce the energy barrier for electrochemical reactions [67]. In a previous study, we slightly removed the rough surface layer of SSP treated AZ31 samples to separate the effect of reduced grain size from that of surface roughness and surface defects on corrosion resistance. The results highlighted the defining role of surface morphology, as the ground samples showed lower corrosion current density compared to the rough surfaces [2]. There is no evidence of a unified theory in the literature on the role of grain refinement in corrosion behaviour, as multiple contradicting data evidence the defining role of the preparation technique, thermal history, corrosive environment, material composition and purity on the corrosion behaviour of nanocrystalline materials [68,69]. There is a general agreement, however, increased dislocation density and grain boundary density in the grain refined layer can increase the surface activity the number of nucleation sites [70,71]. Depending on the environmental, material and process factors, the enhanced surface reactivity will either result in increased degradation or passivation [69].

There are some speculations also on the role of residual stresses on altering the free energy state of plastically deformed materials and their degradation behaviour. There are studies indicating the role of compressive residual stresses in reducing the current density of passivation [72] and increasing corrosion cracking resistance due to the crack closure effect [73]; while other studies report no apparent effect of residual stresses in the degradation behaviour [2,70]. Its effect is recognized as a competition between enhancing the surface reactivity and reducing the risk of defect formation in the oxide layer [69]. The data in the literature suggest that the effect of residual stresses can be dependent on their type and extent the inducing treatment, alloy type and the corrosive environment [70]. Another parameter that could potentially affect the corrosion behaviour and oxide formation is grain orientation and texturing [69,74]. Performing an optimized annealing heat treatment that would relax the residual stresses and cause grain recrystallization could potentially eliminate the effect of all parameters and make it possible to study the sole effect of surface roughness on the corrosion behaviour. Defining this annealing cycle and evaluating its functionality is the subject of future studies.

This increased degradation rate of pure iron can promote its wider application for hard tissue implants, particularly for thin elements such as cardiovascular temporary stents, where the thickness of the affected layer by SSP can be comparable to the wall thickness of the implant; it should be also considered that the depth of the grain refined layer, the work hardened and the layer affected by compressive residual stresses can be modulated by the suitable choice of process parameters and thus can be adjusted to some extent to the target geometry. Our previous studies have confirmed no cytotoxicity effects induced by SSP on different biocompatible metallic materials; furthermore, the induced surface roughness was found effective in promoting osteoblast adhesion and spreading while hindering early stage gram-positive bacteria adhesion. However, if planned to be used for cardiovascular applications, the interaction of the SSP induced surface roughness on pure iron with endothelial cells should be investigated to rule out any risk of cytotoxicity or thrombosis.

5. Conclusions

Severe shot peening results in the formation of a plastically continuous, elastically homogeneous, interface free gradient grain structure in metallic surfaces. The range of the peening parameters that would promote grain refinement on pure iron was identified using a detailed finite element model of the process, considering accumulated plastic strain as the indicative parameter of grain refinement. Based on the finite element results, multiple sets of parameters that would amplify the kinetic energy of the treatment were considered to experimentally obtain grain refinement. The effect of the gradient surface layer was investigated on the mechanical and electrochemical performance of pure iron samples. The obtained results indicated that severe shot peening, applied with proper parameters, can induce significant surface grain refinement, surface work hardening and deep compressive residual stresses in the top surface layer of pure iron. These characteristics can indicate improved mechanical performance for pure iron, particularly under cyclic loading. The surface wettability of the severe shot peened samples was substantially increased compared to the as-received material thanks to the synergistic effect of the surface morphology and the refined grain structure. The degradation rate of severe shot peened pure iron was accelerated especially at

higher exposure times. The quite high surface roughness induced by severe shot peening enhanced the active surface area exposed to the corrosive environment. The surface micro-cracks acted as preferential corrosion sites; furthermore, the grain refined surface layer was found to be more electrochemically active and thus prone to the rapid formation of a corrosion product layer over time. Under longer exposure times, the high extent of corrosion at the surface led to the breakdown and detachment of the protective layer. Thus the substrate was exposed to the corrosive environment again, and consequently, the corrosion rate was accelerated. Whereas, the as-received material, exhibited a stable uniform corrosion product layer firmly adhered to its rather smooth surface.

Based on the obtained results, severe shot peening can be recognized as an efficient surface treatment able to enhance mechanical performance and accelerate the degradation rate of pure iron boosting its broader application for hard tissue implants. Our previous studies have confirmed no cytotoxicity effect induced by severe shot peening on different biocompatible metallic materials; furthermore, the induced surface roughness was found effective in promoting osteoblast adhesion and spreading while hindering early stage gram-positive bacteria adhesion.

Acknowledgments

The authors are grateful to Dr. Michele Bandini of Peenservice srl (IT), for the shot peening treatments. We would like to thank Dr. Monica Moscatelli, of Department of Chemistry, Materials and Chemical Engineering "Giulio Natta" in Politecnico di Milano, for WCA measurements. D.K. and B.H. acknowledge financial support from the Science Grant Agency of the Slovak Republic through project No. 1/0045/17 and the Slovak Research and Development Agency through project No. APVV-16-0276.

Appendix A. Supplementary data

Supplementary data to this article can be found online at https://doi.org/10.1016/j.actbio.2019.05.033.

References

[1] F. Witte, N. Hort, C. Vogt, S. Cohen, K.U. Kainer, R. Willumeit, F. Feyerabend, Degradable biomaterials based on magnesium corrosion, Curr. Opin. Solid State Mater. Sci. 12 (2008) 63–72.
[2] S. Bagherifard, D.J. Hickey, S. Fintová, F. Pastorek, I. Fernandez-Pariente, M. Bandini, T.J. Webster, M. Guagliano, Effects of nanofeatures induced by severe shot peening (SSP) on mechanical, corrosion and cytocompatibility properties of magnesium alloy AZ31, Acta Biomater. 66 (2018) 93–108.
[3] M. Peron, J. Torgersen, F. Berto, Mg and its alloys for biomedical applications: exploring corrosion and its interplay with mechanical failure, Metals 7 (2017) 252.
[4] F. Witte, The history of biodegradable magnesium implants: a review, Acta Biomater. 6 (2010) 1680–1692.
[5] H. Hermawan, D. Dubé, D. Mantovani, Developments in metallic biodegradable stents, Acta Biomaterialia 6 (2010) 1693–1697.
[6] T. Kraus, F. Moszner, S. Fischerauer, M. Fiedler, E. Martinelli, J. Eichler, F. Witte, E. Willbold, M. Schinhammer, M. Meischel, Biodegradable Fe-based alloys for use in osteosynthesis: outcome of an in vivo study after 52 weeks, Acta Biomater. 10 (2014) 3346–3353.
[7] A.H.M. Yusop, N.M. Daud, H. Nur, M.R.A. Kadir, H. Hermawan, Controlling the degradation kinetics of porous iron by poly (lactic-co-glycolic acid) infiltration for use as temporary medical implants, Sci. Rep. (2015) 5.
[8] M. Peuster, P. Wohlsein, M. Brügmann, M. Ehlerding, K. Seidler, C. Fink, H. Brauer, A. Fischer, G. Hausdorf, A novel approach to temporary stenting: degradable cardiovascular stents produced from corrodible metal—results 6–18 months after implantation into New Zealand white rabbits, Heart 86 (2001) 563–569.
[9] P.W. Serruys, M.J. Kutryk, A.T. Ong, Coronary-artery stents, N. Engl. J. Med. 354 (2006) 483–495.
[10] B. Liu, Y. Zheng, Effects of alloying elements (Mn Co, Al, W, Sn, B, C and S) on biodegradability and in vitro biocompatibility of pure iron, Acta Biomater. 7 (2011) 1407–1420.
[11] M. Schinhammer, P. Steiger, F. Moszner, J.F. Löffler, P.J. Uggowitzer, Degradation performance of biodegradable FeMnC (Pd) alloys, Mater. Sci. Eng., C 33 (2013) 1882–1893.
[12] M. Schinhammer, A.C. Hänzi, J.F. Löffler, P.J. Uggowitzer, Design strategy for biodegradable Fe-based alloys for medical applications, Acta Biomater. 6 (2010) 1705–1713.
[13] C.S. Obayi, R. Tolouei, C. Paternoster, S. Turgeon, B.A. Okorie, D.O. Obikwelu, G. Cassar, J. Buhagiar, D. Mantovani, Influence of cross-rolling on the microtexture and biodegradation of pure iron as biodegradable material for medical implants, Acta Biomater. 17 (2015) 68–77.
[14] M. Moravej, A. Purnama, M. Fiset, J. Couet, D. Mantovani, Electroformed pure iron as a new biomaterial for degradable stents: in vitro degradation and preliminary cell viability studies, Acta Biomater. 6 (2010) 1843–1851.
[15] A.H.M. Yusop, N.M. Daud, H. Nur, M.R.A. Kadir, H. Hermawan, Controlling the degradation kinetics of porous iron by poly (lactic-co-glycolic acid) infiltration for use as temporary medical implants, Sci. Rep. 5 (2015) 11194.
[16] J. Cheng, T. Huang, Y. Zheng, Relatively uniform and accelerated degradation of pure iron coated with micro-patterned Au disc arrays, Mater. Sci. Eng., C 48 (2015) 679–687.
[17] T. Huang, Y. Zheng, Uniform and accelerated degradation of pure iron patterned by Pt disc arrays, Sci. Rep. 6 (2016) 23627.
[18] S. Zhu, N. Huang, L. Xu, Y. Zhang, H. Liu, Y. Lei, H. Sun, Y. Yao, Biocompatibility of Fe–O films synthesized by plasma immersion ion implantation and deposition, Surf. Coat. Technol. 203 (2009) 1523–1529.
[19] S. Zhu, N. Huang, H. Shu, Y. Wu, L. Xu, Corrosion resistance and blood compatibility of lanthanum ion implanted pure iron by MEVVA, Appl. Surf. Sci. 256 (2009) 99–104.
[20] H. Chen, E. Zhang, K. Yang, Microstructure, corrosion properties and biocompatibility of calcium zinc phosphate coating on pure iron for biomedical application, Mater. Sci. Eng., C 34 (2014) 201–206.
[21] S. Bagherifard, I. Fernandez-Pariente, R. Ghelichi, M. Guagliano, in: Process and Properties of the Treated Surfaces: Handbook of Mechanical Nanostructuring. Severe Shot Peening to Obtain Nanostructured Surfaces, 2015, pp. 299–323.
[22] S. Bagheri, M. Guagliano, Review of shot peening processes to obtain nanocrystalline surfaces in metal alloys, Surf. Eng. 25 (2009) 3–14.
[23] F. Yin, R. Xu, S. Hu, K. Zhao, S. Yang, S. Kuang, Q. Li, Q. Han, Enhanced mechanical and biological performance of an extremely fine nanograined 316L stainless steel cell-substrate interface fabricated by ultrasonic shot peening, ACS Biomater. Sci. Eng. 4 (2018) 1609–1621.
[24] S. Bahl, S.R.K. Meka, S. Suwas, Chatterjee K. Surface, Severe plastic deformation of an orthopedic Ti–Nb–Sn alloy induces unusual precipitate remodeling and supports stem cell osteogenesis through Akt signaling, ACS Biomater. Sci. Eng. (2018).
[25] D.V. Nazarov, V.M. Smirnov, E.G. Zemtsova, N.M. Yudintceva, M.A. Shevtsov, R. Z. Valiev, Enhanced osseointegrative properties of ultra-fine-grained titanium implants modified by chemical etching and atomic layer deposition, ACS Biomater. Sci. Eng. 4 (2018) 3268–3281.
[26] G. Perumal, A. Ayyagari, A. Chakrabarti, D. Kannan, S. Pati, H.S. Grewal, S. Mukherjee, S. Singh, H.S. Arora, Friction stir processing of stainless steel for ascertaining its superlative performance in bioimplant applications, ACS Appl. Mater. Interfaces 9 (2017) 36615–36631.
[27] S. Bagherifard, R. Ghelichi, A. Khademhosseini, M. Guagliano, Cell response to nanocrystallized metallic substrates obtained through severe plastic deformation, ACS Appl. Mater. Interfaces 6 (2014) 7963–7985.
[28] S. Bagherifard, M. Guagliano, Fatigue behavior of a low-alloy steel with nanostructured surface obtained by severe shot peening, Eng. Fract. Mech. 81 (2012) 56–68.
[29] S. Bagherifard, I. Fernandez-Pariente, R. Ghelichi, M. Guagliano, Fatigue behavior of notched steel specimens with nanocrystallized surface obtained by severe shot peening, Mater. Des. 45 (2013) 497–503.
[30] M. Palacios, S. Bagherifard, M. Guagliano, Pariente I. Fernández, Influence of severe shot peening on wear behaviour of an aluminium alloy, Fatigue Fract. Eng. Mater. Struct. 37 (2014) 821–829.
[31] S. Bagherifard, S. Slawik, I. Fernández-Pariente, C. Pauly, F. Mücklich, M. Guagliano, Nanoscale surface modification of AISI 316L stainless steel by severe shot peening, Mater. Des. 102 (2016) 68–77.
[32] S. Bagherifard, I. Fernandez-Pariente, R. Ghelichi, M. Guagliano, Effect of severe shot peening on microstructure and fatigue strength of cast iron, Int. J. Fatigue 65 (2014) 64–70.
[33] S. Bagherifard, D.J. Hickey, A.C. de Luca, V.N. Malheiro, A.E. Markaki, M. Guagliano, T.J. Webster, The influence of nanostructured features on bacterial adhesion and bone cell functions on severely shot peened 316L stainless steel, Biomaterials 73 (2015) 185–197.
[34] N. Tao, M. Sui, J. Lu, K. Lua, Surface nanocrystallization of iron induced by ultrasonic shot peening, Nanostruct. Mater. 11 (1999) 433–440.
[35] N. Tao, Z. Wang, W. Tong, M. Sui, J. Lu, K. Lu, An investigation of surface nanocrystallization mechanism in Fe induced by surface mechanical attrition treatment, Acta Mater. 50 (2002) 4603–4616.
[36] K. Lu, J. Lu, Nanostructured surface layer on metallic materials induced by surface mechanical attrition treatment, Mater. Sci. Eng., A 375–377 (2004) 38–45.
[37] H.A. Murdoch, K.A. Darling, A.J. Roberts, L. Kecskes, Mechanical behavior of ultrafine gradient grain structures produced via ambient and cryogenic surface mechanical attrition treatment in iron, Metals 5 (2015) 976–985.
[38] V. Lacaille, G. Kermouche, D.T. Spinel, E. Feulvarch, C. Morel, J. Bergheau, Modeling nitriding enhancement resulting from the NanoPeening treatment of

a Pure Iron, IOP Conference Series: Materials Science and Engineering, IOP Publishing, 2014.
[39] D. Tumbajoy-Spinel, S. Descartes, J.-M. Bergheau, V. Lacaille, G. Guillonneau, J. Michler, G. Kermouche, Assessment of mechanical property gradients after impact-based surface treatment: application to pure α-iron, Mater. Sci. Eng., A 667 (2016) 189–198.
[40] Y. Kaneko, T. Sugimoto, EBSD analysis of microstructure evolution of pure iron subjected to sliding wear and related change in Vickers microhardness, Mater. Trans. 55 (2014) 85–92.
[41] S. Bagherifard, R. Ghelichi, M. Guagliano, On the shot peening surface coverage and its assessment by means of finite element simulation: a critical review and some original developments, Appl. Surf. Sci. 259 (2012) 186–194.
[42] G.R. Johnson, A constitutive model and data for materials subjected to large strains, high strain rates, and high temperatures, in: Proc 7th Inf Sympo Ballistics, 1983, pp. 541–547.
[43] G. Carter, R. Hooper, J. Henshall, M. Guillou, Friction of metal sliders on toughened zirconia ceramic between 298 and 973 K, Wear 148 (1991) 147–160.
[44] S. Bagherifard, R. Ghelichi, M. Guagliano, A numerical model of severe shot peening (SSP) to predict the generation of a nanostructured surface layer of material, Surf. Coat. Technol. 204 (2010) 4081–4090.
[45] A. Heydari Astaraee, R. Miresmaeili, S. Bagherifard, M. Guagliano, M. Aliofkhazraei, Incorporating the principles of shot peening for a better understanding of surface mechanical attrition treatment (SMAT) by simulations and experiments, Mater. Des. 116 (2017) 365–373.
[46] J.N. Li, P. Cao, X.N. Zhang, S.X. Zhang, Y.H. He, In vitro degradation and cell attachment of a PLGA coated biodegradable Mg–6Zn based alloy, J. Mater. Sci. 45 (2010) 6038–6045.
[47] G. Wang, S. Ge, Y. Shen, H. Wang, Q. Dong, Q. Zhang, J. Gao, Y. Wang, Study on the biodegradability and biocompatibility of WE magnesium alloys, Mater. Sci. Eng., C 32 (2012) 2190–2198.
[48] N. Saikrishna, G. Pradeep Kumar Reddy, B. Munirathinam, Ratna Sunil B. Influence of bimodal grain size distribution on the corrosion behavior of friction stir processed biodegradable AZ31 magnesium alloy, J. Magnesium Alloys 4 (2016) 68–76.
[49] A.H. Volume, 13A, Corrosion: Fundamentals, Testing, and Protection, ASM International, 2003.
[50] R. Ghelichi, G. Crispiatico, M. Guagliano, S. Bagherifard, An energetic approach to predict the effect of shot peening-based surface treatments, Metals 8 (2018) 190.
[51] M. Umemoto, Y. Todaka, K. Tsuchiya, Formation of nanocrystalline structure in steels by air blast shot peening, Mater. Trans. 44 (2003) 1488–1493.
[52] R. Valiev, Nanostructuring of metals by severe plastic deformation for advanced properties, Nat. Mater. 3 (2004) 511.
[53] A. Ranella, M. Barberoglou, S. Bakogianni, C. Fotakis, E. Stratakis, Tuning cell adhesion by controlling the roughness and wettability of 3D micro/nano silicon structures, Acta Biomater. 6 (2010) 2711–2720.
[54] S. Bauer, J. Park, Mark Kvd, P. Schmuki, Improved attachment of mesenchymal stem cells on super-hydrophobic TiO2 nanotubes, Acta Biomater. 4 (2008) 1576–1582.
[55] M. Padial-Molina, P. Galindo-Moreno, J.E. Fernández-Barbero, F. O'Valle, A.B. Jódar-Reyes, J.L. Ortega-Vinuesa, P.J. Ramón-Torregrosa, Role of wettability and nanoroughness on interactions between osteoblast and modified silicon surfaces, Acta Biomater. 7 (2011) 771–778.
[56] M. Bigerelle, K. Anselme, Statistical correlation between cell adhesion and proliferation on biocompatible metallic materials, J. Biomed. Mater. Res. Part A 72 (2005) 36–46.
[57] K. Lu, J. Lu, Nanostructured surface layer on metallic materials induced by surface mechanical attrition treatment, Mater. Sci. Eng., A 375 (2004) 38–45.
[58] D. Kuhlmann-Wilsdorf, J. Van der Merwe, Theory of dislocation cell sizes in deformed metals, Mater. Sci. Eng. 55 (1982) 79–83.
[59] D. Tumbajoy-Spinel, S. Descartes, J.-M. Bergheau, H. Al-Baida, C. Langlade, G. Kermouche, Investigation of graded strengthened hyper-deformed surfaces by impact treatment: micro-percussion testing, IOP Conference Series: Materials Science and Engineering, IOP Publishing, 2017. 012024.
[60] J. Yin, M. Umemoto, K. Tsuchiya, Formation mechanism and annealing behavior of nanocrystalline ferrite in pure Fe fabricated by ball milling, ISIJ Int. 41 (2001) 1389–1396.
[61] S. Bagherifard, N. Beretta, S. Monti, M. Riccio, M. Bandini, M. Guagliano, On the fatigue strength enhancement of additive manufactured AlSi10Mg parts by mechanical and thermal post-processing, Mater. Des. 145 (2018) 28–41.
[62] S. Fintova, L. Kunz, Fatigue properties of magnesium alloy AZ91 processed by severe plastic deformation, J. Mech. Behav. Biomed. Mater. 42 (2015) 219–228.
[63] M. Vashista, S. Paul, Correlation between full width at half maximum (FWHM) of XRD peak with residual stress on ground surfaces, Phil. Mag. 92 (2012) 4194–4204.
[64] J. Zhou, Y. Yang, M. Alonso Frank, R. Detsch, A.R. Boccaccini, S. Virtanen, Accelerated degradation behavior and cytocompatibility of pure iron treated with sandblasting, ACS Appl. Mater. Interfaces 8 (2016) 26482–26492.
[65] A. Amirudin, D. Thieny, Application of electrochemical impedance spectroscopy to study the degradation of polymer-coated metals, Prog. Org. Coat. 26 (1995) 1–28.
[66] PalmSens. https://wwwpalmsenscorrosioncom/knowledgebase/equivalent-circuit-fitting-corrosion-measurements 2019.
[67] W. Li, D. Li, Variations of work function and corrosion behaviors of deformed copper surfaces, Appl. Surf. Sci. 240 (2005) 388–395.
[68] S.G. Wang, C.B. Shen, K. Long, H.Y. Yang, F.H. Wang, Z.D. Zhang, Preparation and electrochemical corrosion behavior of bulk nanocrystalline ingot iron in HCl acid solution, J. Phys. Chem. B 109 (2005) 2499–2503.
[69] K. Ralston, N. Birbilis, Effect of grain size on corrosion: a review, Corrosion 66 (2010) 075005–75013.
[70] B. Thangaraj, T.S. Nellaiappan, S. Narayanan, R. Kulandaivelu, M.H. Lee, T. Nishimura, A facile method to modify the characteristics and corrosion behavior of 304 stainless steel by surface nanostructuring toward biomedical applications, ACS Appl. Mater. Interfaces 7 (2015) 17731–17747.
[71] N. Greene, G. Saltzman, Effect of plastic deformation on the corrosion of iron and steel, Corrosion 20 (1964) 293t–298t.
[72] O. Takakuwa, H. Soyama, Effect of residual stress on the corrosion behavior of austenitic stainless steel, Adv. Chem. Eng. Sci. 5 (2015) 62–71.
[73] N. Winzer, A. Atrens, G. Song, E. Ghali, W. Dietzel, K.U. Kainer, N. Hort, C. Blawert, A critical review of the stress corrosion cracking (SCC) of magnesium alloys, Adv. Eng. Mater. 7 (2005) 659–693.
[74] M. Moravej, S. Amira, F. Prima, A. Rahem, M. Fiset, D. Mantovani, Effect of electrodeposition current density on the microstructure and the degradation of electroformed iron for degradable stents, Mater. Sci. Eng., B 176 (2011) 1812–1822.